

## Supporting Information

# Engineering Shadows to Fabricate Optical Metasurfaces

*Alex Nemiroski<sup>1</sup>, Mathieu Gonidec<sup>1</sup>, Jerome Fox<sup>1</sup>, Philip Jean-Remy<sup>1</sup>, Evan Turnage<sup>1</sup>,*

*and George M. Whitesides<sup>1,2,3\*</sup>*

<sup>1</sup>Department of Chemistry & Chemical Biology, <sup>2</sup>Wyss Institute for Biologically Inspired Engineering, <sup>3</sup>The Kavli Insitute for Bionano Science, Harvard University,  
Cambridge, Massachussetts 02138, United States

\*Address correspondence to: [gwhitesides@gmwgroup.harvard.edu](mailto:gwhitesides@gmwgroup.harvard.edu).

## SUPPLEMENTARY BACKGROUND AND MODELING OF SHADOWS

### Expanded Background on Nanosphere Lithography

Shadowed deposition through MCCs—known as nanosphere (NSL) or colloidal lithography—has thus far been limited to a very narrow range of possible patterns such as triangular nanoparticles,<sup>1-3</sup> nanowires,<sup>4</sup> nano-rings and nano-crescents.<sup>5,6</sup> Further etching of these types of structures has also been used to create arrays of nanoholes<sup>7</sup> and pillars.<sup>8</sup> Only a very small fraction of the available parameter space has been explored and no method has ever been previously presented that enables the design of new, complex nanostructures.

### Modeling Shadows

For a planar source at polar angle  $\theta$  (inclination from z-axis) and azimuthal angle  $\phi$  (counter clockwise rotation from x-axis, in the x/y plane), the shadow cast onto the x-y plane by a sphere of radius  $r$  located at  $(x, y) = (0, 0)$  and resting on the plane, is that of an ellipse with a major radius  $a = r \sec \theta$  and minor radius  $b = r$  (Figure S1). The ellipse is rotated by  $\phi$  around the origin and centered at  $(x, y) = (-r \tan \theta \cos \phi, -r \tan \theta \sin \phi)$ . The distance from the origin to center of the ellipse is

$$f = \sqrt{(r \tan \theta \cos \phi)^2 + (r \tan \theta \sin \phi)^2} = r \tan \theta = \sqrt{a^2 - b^2}, \quad (1)$$

which is the distance from the center of the ellipse a focus. As the azimuthal angle  $\phi$  of the projecting source changes, the elliptical shadow rotates about the focus proximal to the source.

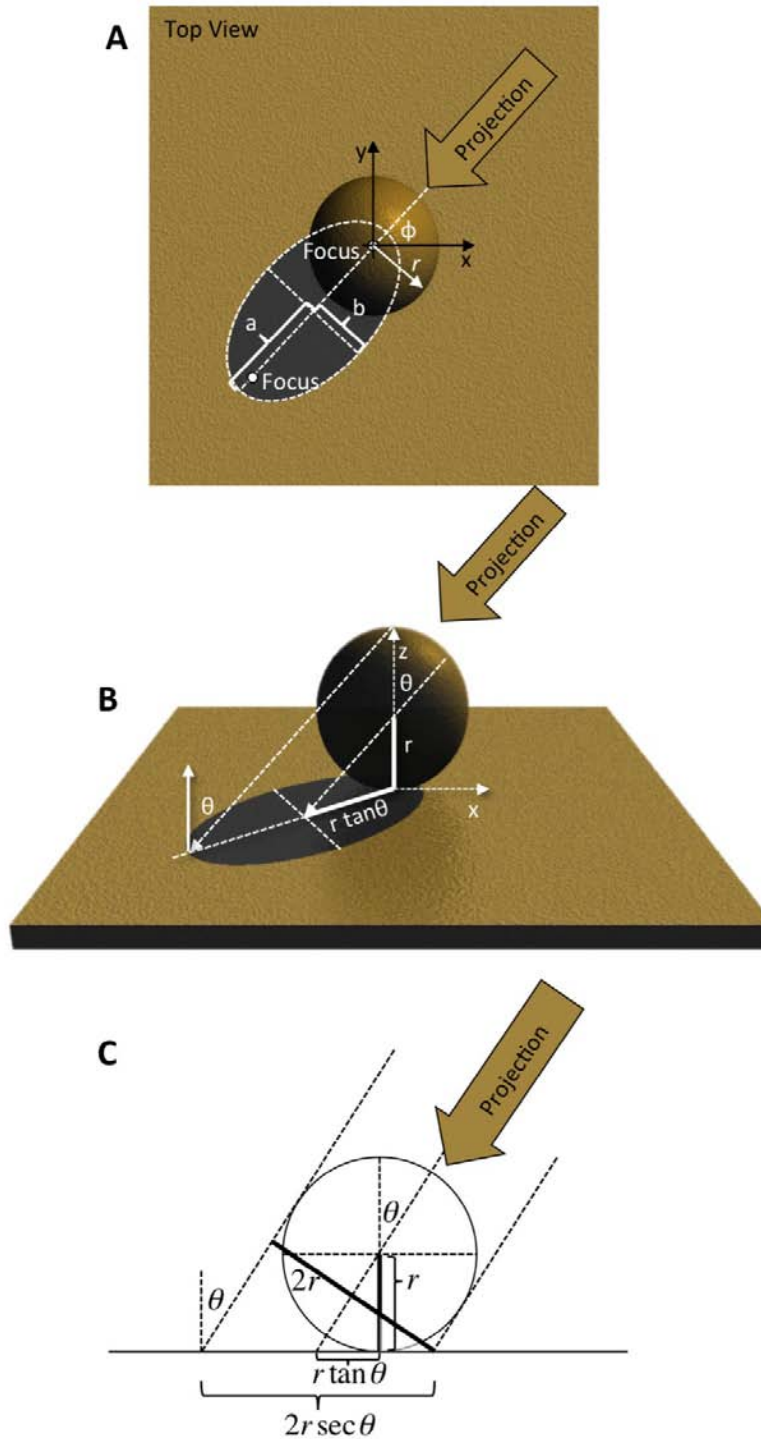


**Figure S1.** Depiction of elliptical shadow cause by a sphere at (0, 0) with a projection source at angle  $(\theta, \phi)$ . a) The top view. b) A front, angled view. c) A schematic detailing the trigonometry.

## Classes of Shadows for a Single Angle of Projection

Figure S2 shows the five classes of shapes that occur within the parameter space of shadows: i) isolated triangles, ii) honeycomb lattice, iii) interconnected lines, iv) antisymmetric bars, and iv) symmetric bars. A lattice of triangles is formed at normal incidence with no gap (no etching, spheres are close-packed). A honeycomb lattice is formed at normal incidence for finite gap (some etching). The interesting isolated structures tend to appear, in general, at intermediate polar angles ( $\theta = 30^\circ - 60^\circ$ ). Within this regime, interconnected lines are formed for azimuthal angles near  $\phi \approx 0^\circ + n \cdot 60^\circ$ , asymmetric bars for angles near  $\phi \approx 15^\circ + n \cdot 30^\circ$ , and symmetric bars only at angles  $\phi = 30^\circ + n \cdot 60^\circ$ , where  $n \in \text{integers}$ . As the azimuthal angle  $\phi$  is swept at constant  $\theta$ , the features transition smoothly from lines to asymmetric bars, to symmetric bars and back again. A theoretical treatment for a single angle of projection has been recently presented by Kostinski et al.<sup>9</sup> in collaboration with this effort.

Eventually as the polar angle  $\theta$  is increased further to oblique angles, the interconnected lines break apart into isolated, oblique triangles. Beyond  $\theta \sim 65^\circ$ , the spheres tend to obscure the entire substrate. The exact angles at which different classes of patterns transition from one to another depend exclusively on the ratio between the gap  $g$  between spheres and the pitch  $p$  of the array ( $g/p$ ). The length and width of each feature is controlled by varying the gap size and  $\theta$ . Although both of these parameters affect the length/width, we have found that when designing structures, the gap is most closely linked to the overall width of features and the angle  $\theta$  most closely linked to the length of each feature.

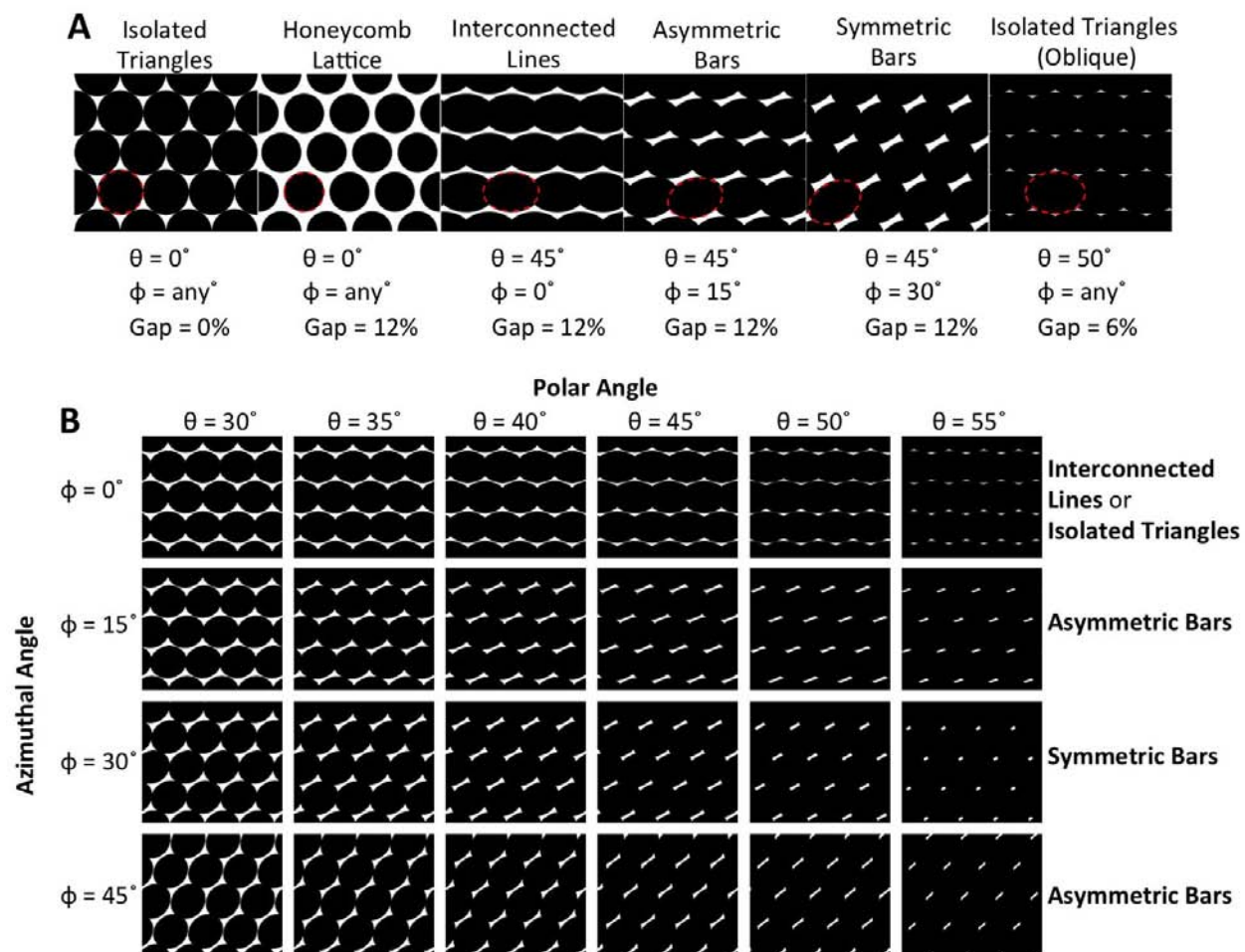


**Figure S2.** Some typical features formed from a single angle of projection. a) The five possible types of shadows along with typical angles and gaps at which they occur. In each case, a single shadow is highlighted by the red dotted line. b) Examples of lines, bars, and oblique triangles for intermediate polar angles. We depict a sample of features along lines of high crystal symmetry. Each feature is reproduced at  $\phi = 60^\circ$  increments (not shown). All images were generated in Mathematica.

## Software for Designing Metasurfaces by Overlapping Multiple Shadows

We designed the Mathematica-based software (Figures S3-S4) to generate a hexagonal array of elliptical shadows parameterized by four types of input parameters: pitch  $p$  of the array, gap  $g$  between spheres, and angles of projection  $(\theta_i, \phi_i)$  for each source. The software considers each angle of projection separately. It constructs the shadow pattern from a single projection by (i) defining an origin; (ii) creating a single, black, elliptical shadow with dimensions

$a = \frac{p-g}{2} \sec \theta_i$  and  $b = \frac{p-g}{2}$  centered at the origin; (iii) displacing the ellipse from the origin by  $(-\frac{p}{2} \tan \theta, 0)$ ; and then iv) rotating the ellipse counter-clockwise about the origin point by  $\phi_i$ .

Next, the software creates a hexagonal array of these ellipses. The resulting pattern is equivalent to the shadow formed by a hexagonally non-close-packed array of spheres with pitch  $p$  and radii  $r = b$  cast from a single angle of projection  $(\theta_i, \phi_i)$ . Finally, to overlap multiple angles of projection, the software performs a Boolean OR operation between images of all the individually generated patterns.

Figure S3 shows a screen-shot of the “SSL Artist” software that we developed. We have made a web-based version available at [http://gmwgroup.harvard.edu/science/SSL\\_artist/](http://gmwgroup.harvard.edu/science/SSL_artist/) (running SSL Artist requires either Mathematica, or the free Wolfram CDF Player, available at <https://www.wolfram.com/cdf-player/>). At the conclusion of design, the software outputs the parameters required for fabrication: colloidal diameter  $d = p$ , etching time  $t = Cg/2$ , and stage angles  $[\theta_i, \phi_i]$  for each sequential deposition, where  $C$  is the calibrated etch-rate of polystyrene for the oxygen plasma. For a plasma generated by 50W RF power and an O<sub>2</sub> flow-rate of 3 sccm, we determined  $C = 10$  s/nm. Following the completion of a design, these parameters, along with the desired thickness for each feature and choice materials, formed a complete set of parameters required to fabricate all structures.

## SSL Artist

Created by Alex Nemiroski (anemiroski@gmwgroup.harvard.edu) 2014

### Global Controls

Display Sources:

Active Sources:

Template: Chiral Hexapole (point group C<sub>6</sub>) 

Pitch:

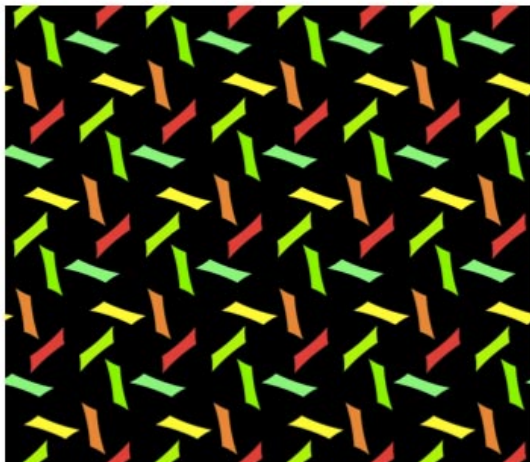
Gap:

Azimuthal Offset ( $\phi_0$ ):

Polar Offset ( $\theta_0$ ):

### Local Angle Controls

<input type="checkbox"/> Azimuthal Angle ( $\phi_1$ )	<input type="range"/>	<input type="text" value="45°"/>	<input type="checkbox"/> Polar Angle ( $\theta_1$ )	<input type="range"/>	<input type="text" value="54°"/>
<input type="checkbox"/> Azimuthal Angle ( $\phi_2$ )	<input type="range"/>	<input type="text" value="105°"/>	<input type="checkbox"/> Polar Angle ( $\theta_2$ )	<input type="range"/>	<input type="text" value="54°"/>
<input type="checkbox"/> Azimuthal Angle ( $\phi_3$ )	<input type="range"/>	<input type="text" value="165°"/>	<input type="checkbox"/> Polar Angle ( $\theta_3$ )	<input type="range"/>	<input type="text" value="54°"/>
<input type="checkbox"/> Azimuthal Angle ( $\phi_4$ )	<input type="range"/>	<input type="text" value="225°"/>	<input type="checkbox"/> Polar Angle ( $\theta_4$ )	<input type="range"/>	<input type="text" value="54°"/>
<input type="checkbox"/> Azimuthal Angle ( $\phi_5$ )	<input type="range"/>	<input type="text" value="285°"/>	<input type="checkbox"/> Polar Angle ( $\theta_5$ )	<input type="range"/>	<input type="text" value="54°"/>
<input type="checkbox"/> Azimuthal Angle ( $\phi_6$ )	<input type="range"/>	<input type="text" value="345°"/>	<input type="checkbox"/> Polar Angle ( $\theta_6$ )	<input type="range"/>	<input type="text" value="54°"/>



#### OUTPUT

Colloidal Diameter: 1000 nm  
Etch: 50 nm (Etch Time = 8.3 min @ 3ccm O<sub>2</sub>, 50W)  
Deposition Angles ( $\phi, \theta$ )  
#1 (45°, 54°)  
#2 (105°, 54°)  
#3 (165°, 54°)  
#4 (225°, 54°)  
#5 (285°, 54°)  
#6 (345°, 54°)

**Figure S3.** A screen-shot of the Mathematica-based software (SSL Artist) that we developed to aid in the rapid design of nanoantennas with SSL. Here, we show the design for a chiral-hexapole antenna with C<sub>6</sub> symmetry formed by six angles of projection. The software enables the simulation of up to 12 independent sources (although more is possible). The sliders control all simulated angles of projection in real-time. The azimuthal  $\phi_0$  and polar  $\theta_0$  offsets are global parameters that can be added to all sources simultaneously. Here we (i) designed the structure to have C<sub>6</sub> symmetry by first specifying  $\phi_i = \phi_0 + n_i \cdot 60^\circ$ , then we (ii) tuned  $\theta$  until the length of the arms were an adequate length, and finally we (iii) added a global offset  $\phi_0 = 15^\circ$  to all sources to make the structure chiral and disconnected. This structure is saved as the “chiral hexapole” option in a drop down menu.

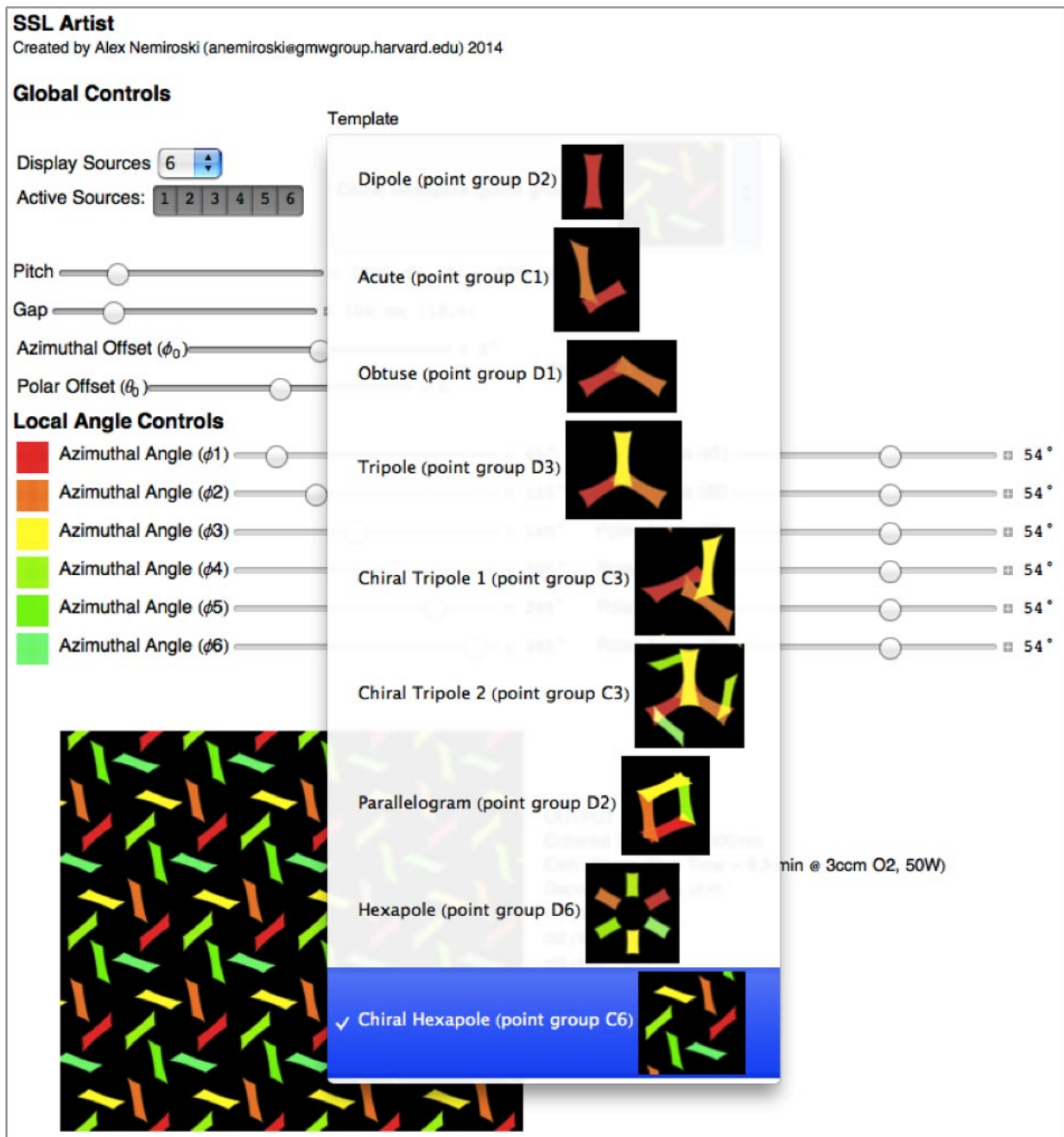


**Figure S4.** A screen-shot of SSL Artist that demonstrates the capability of the software to specify a structure (by name, point group symmetry, or shape) as a starting point for the design of a metasurface.

## SUPPLEMENTARY METHODS AND RESULTS

### Fabrication of Monolayer Colloidal Crystals

We obtained polystyrene (PS) microspheres from Polysciences (Warrington, PA) with 0.99- $\mu\text{m}$  diameter as 2.6% (wt.) latex suspensions. To obtain high quality monolayers, we purified the PS beads suspensions extensively before use by diluting the latex suspensions by 50% in ethanol and centrifuging them at 3000 rpm for 30 minutes. We then discarded the supernatant and re-suspended the pellet of beads in a 1:1 mixture of ethanol in water. We repeated this process at least three times.

To prepare the self-assembled MCCs, we filled disposable, polystyrene petri dishes (150 x 25 mm, Beckton-Dickinson) with a 17- $\mu\text{M}$  aqueous solution of NaOH. We inserted a glass slide (made hydrophilic by treatment with air plasma for five minutes), at a 30° angle between the glass slide and the water meniscus. We then slowly added the suspension to the glass slide, leading to the insertion of the PS microspheres at the air-water interface. The microspheres remained trapped at the air-water interface and assembled into polycrystalline MCCs within minutes. To pick-up the MCCs, we inserted the receiving substrates (typically silicon or glass) underneath the monolayer surface and pulled them out of the water at a shallow angle. We finally dried the samples in ambient conditions at a 45° angle with respect to the vertical direction. We generated 50–120 nm gaps between the spheres by exposing samples for 8–12 minutes to an O<sub>2</sub> plasma etch (Micro Stripper 220, Technics) at 50 W of RF power and 3 sccm of O<sub>2</sub> gas flow. This convenient method, which was primarily based on work done by Vogel *et al.*,<sup>10</sup> formed a polycrystalline MCC with many randomly oriented domains with sizes suitable for optical characterization. In principle, well-oriented, large-area domains (cm<sup>2</sup>) can be formed by other, more sophisticated methods of self-assembly.<sup>11,12</sup>

## Rotation Stage

We constructed a vacuum-compatible, sample rotation stage (Figure S5) with two, independently controlled rotation axes consisting of (i) an aluminum rotation stage (CR-1 custom, Thorlabs) with continuous  $360^\circ$  rotation and  $0.2^\circ$  resolution, to control the azimuthal angle  $\phi$ , and (ii) a stainless steel rotation stage (GOHS-40A35, OptoSigma Corp.) with  $\pm 20^\circ$  range and  $0.2^\circ$  resolution mounted at  $45^\circ$  to the sample/source axis, to control the polar angle  $\theta$ . We assembled the sample stage with a set of custom-built aluminum components, and vented stainless-steel screws (McMaster). We mounted the stage in an electron beam evaporator (Sharon Vacuum Co, Inc.) and used an external knob connected to a manual feed-through and a flexible shaft (McMaster) to precisely ( $\pm 0.5^\circ$ ) control the azimuthal angle of the sample relative to the source. The total cost for materials and fabrication of the rotation stage was  $\sim \$1600$ .

## Deposition

In all cases in which we used Ag, we fabricated devices by first sequentially depositing a nucleation layer (2 nm of Ge at  $1 \text{ \AA/s}$ ) at each angle required from the specified design, and then sequentially depositing the active layer (10–20 nm of Ag at  $1 \text{ \AA/s}$ ) on top of the nucleation layer at each angle required by the design. At the completion of each deposition step (a single deposition at a single angle), we closed the source shutter (while maintaining a constant deposition rate), adjusted the angular control knobs to the next angle, and opened the shutter to continue deposition onto the sample. For devices composed of Au, we performed the same procedure with Ti as the adhesion layer and then Au as the active layer. For optically active devices (Figure 5), we deposited 10 nm of Au at a time for each feature. In each case, after deposition, we removed the polystyrene monolayer with tape (Scotch, 3M).

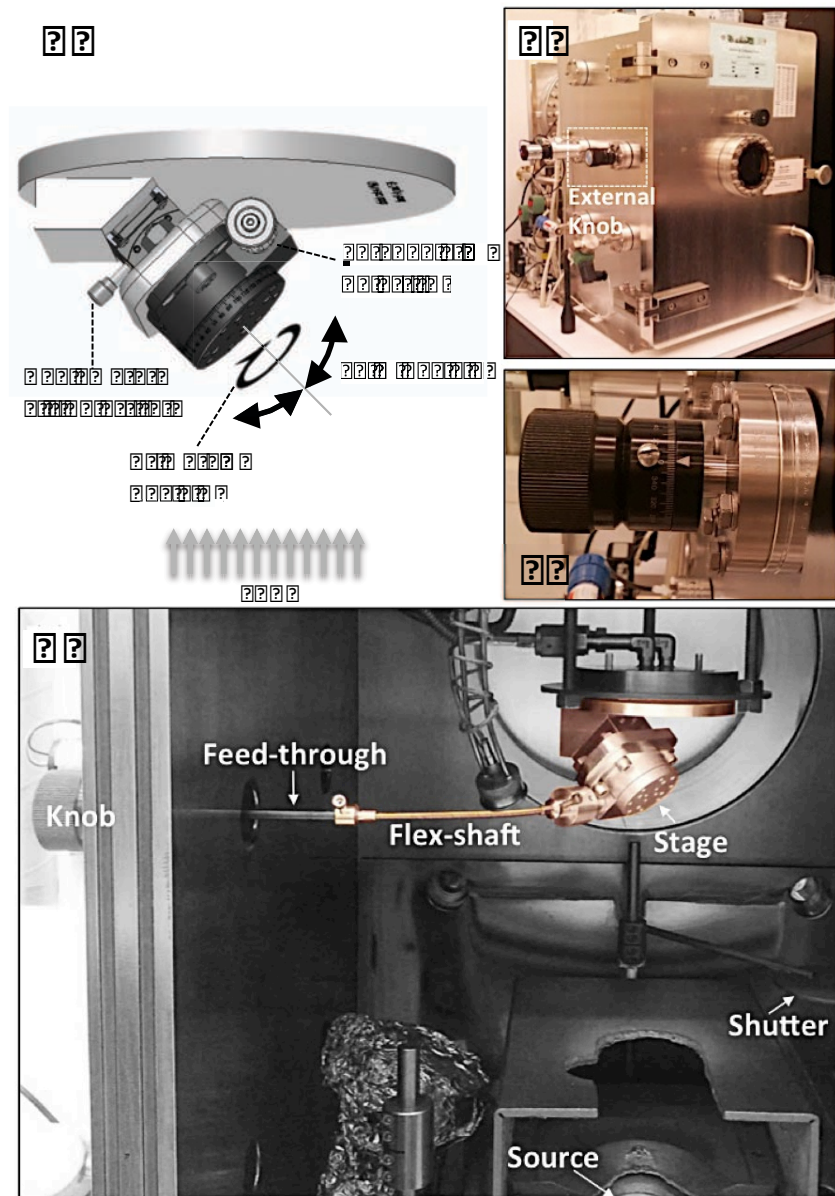


**Figure S5.** The angled deposition system: A) Scheme depicting the assembly of two-axis rotation stage. B) Photograph of the electron beam evaporation system we used. C) Close-up image of the external knob we used to control the azimuthal angle. D) Image showing the rotation stage mounted inside the vacuum chamber and the connection between the external knobs, feed-through, and a flexible shaft. We have altered the image to highlight the components that we built.

## **Additional Images of Multi-material Metasurfaces**

Figure S6 depicts eight different metasurfaces fabricated from multiple materials, including Ag, Au, and Cu.

## **Characterization of Domains**

To quantify the statistics of domain sizes we photographed a representative sample of an MCC formed from 1- $\mu\text{m}$  polystyrene spheres on glass and illuminated with a white light source, and then performed image analysis in Mathematica to identify and count the different single-domains (grains). Figure S7A shows an image of a typical MCC. Each grain diffracts light such that the color within each single domain appears approximately uniform and depends on the rotation of the domain relative to the light source and camera; the sharp color gradient at the grain boundaries enables the grains to be easily identified. Each pixel in the image corresponds to  $16 \times 16 \mu\text{m}^2$ ; domains that are not resolved by the camera, or highly disordered, appear as a tan color. We identified domains by processing the image as follows: (i) we applied a mask configured to remove all areas that did not correspond to either the sample or domains large enough for optical characterization; (ii) we performed a 14-color, clustering algorithm to group neighboring pixels by color; (iii) we applied a single-pixel gradient filter to find the edges of each domain; (iv) we counted the area (number of pixels) circumscribed by the each of each domain; (v) we binned the area of each identified domain and determined the number of areas of each size per  $\text{cm}^2$ . The inset of Figure S7A shows a composite of steps i-iii for a representative region of the sample. Processing the image in this way yielded an average areal density of  $\sim 6000$  domains/ $\text{cm}^2$  of which nearly  $N \sim 2000$  had a domain area  $a > 100 \times 100 \mu\text{m}^2$ .

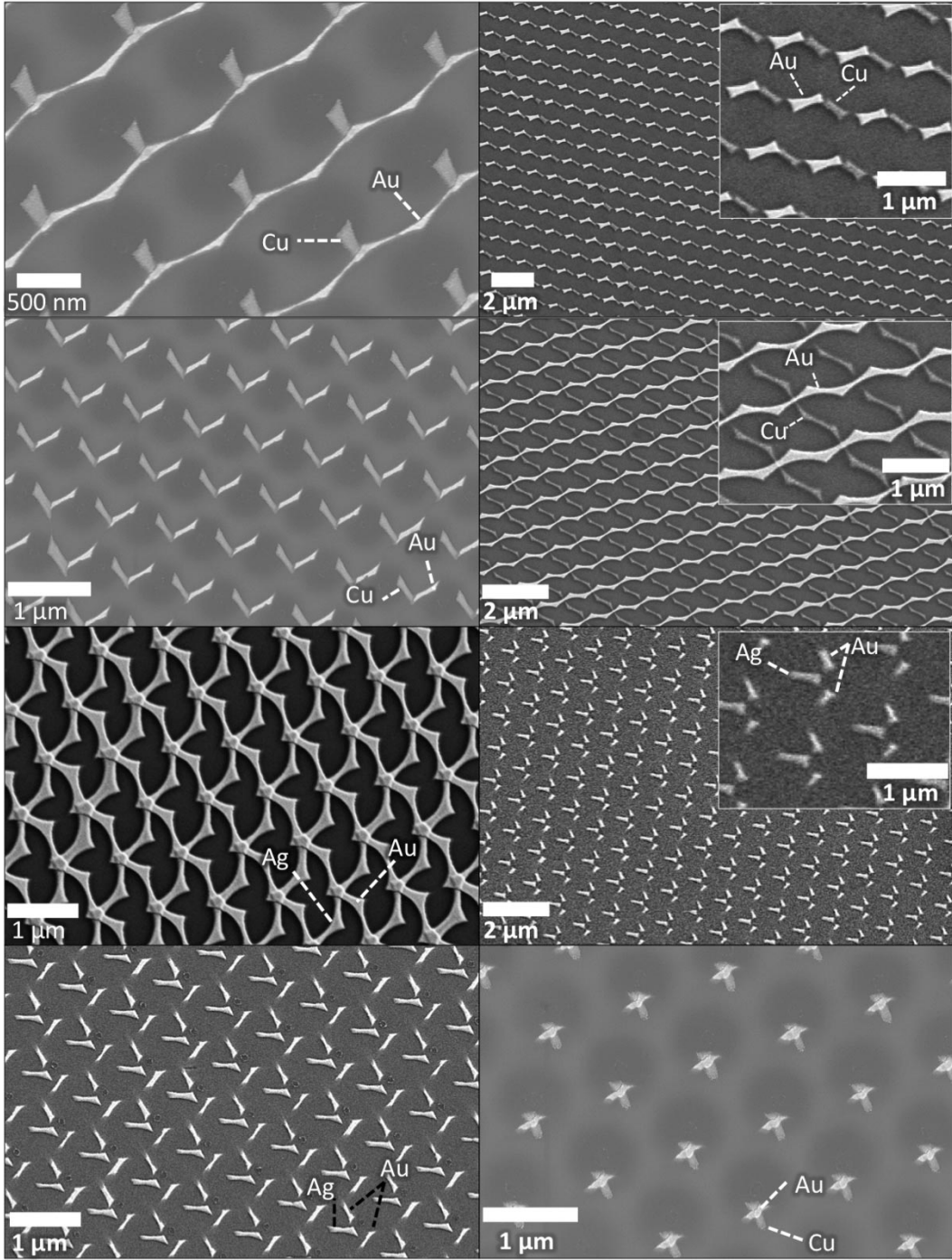


**Figure S6.** Assorted multi-material devices fabricated with 2–3 different angles of deposition. We use Ti as an adhesion layer for Au, and Ge as a nucleation layer for Ag.

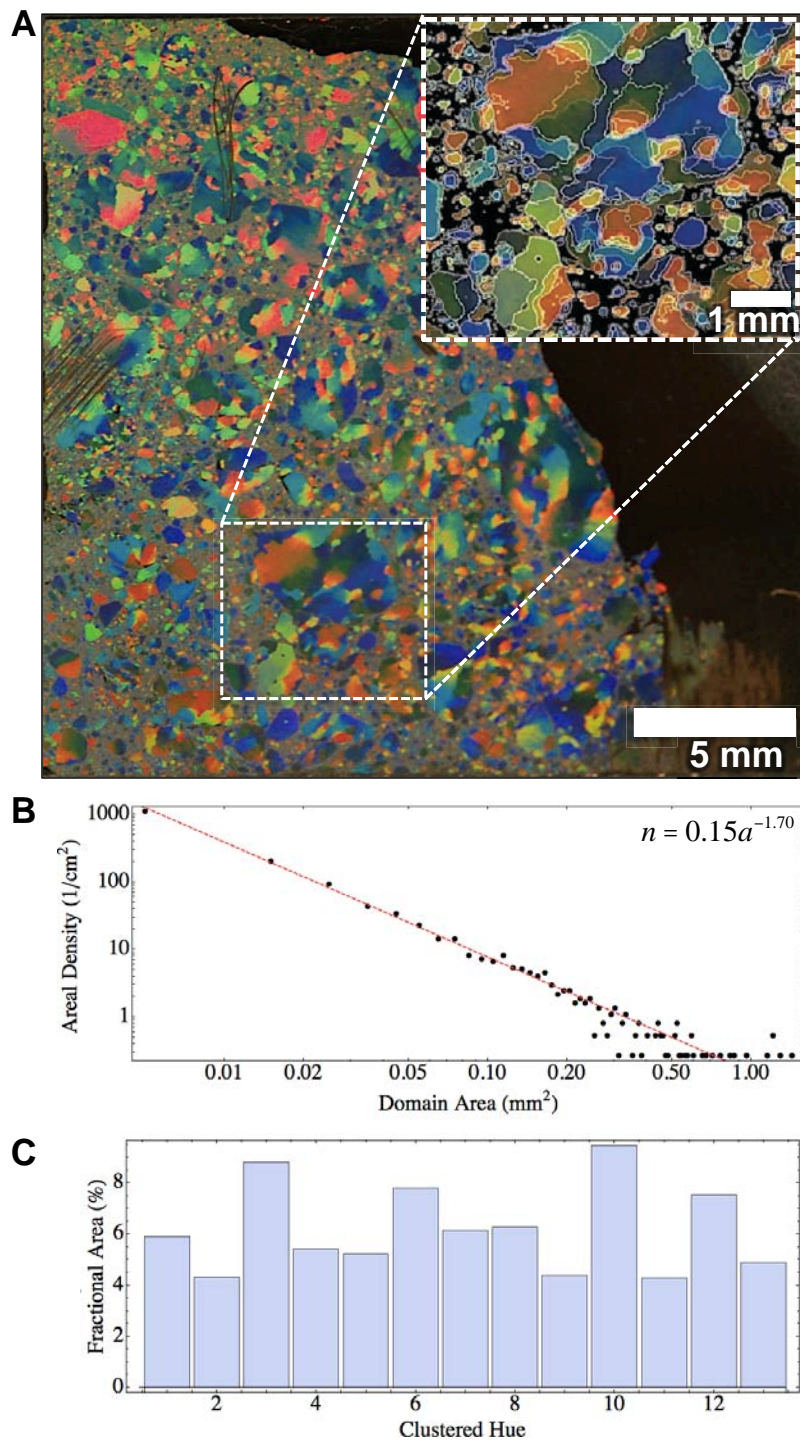


**Figure S7.** A) Photograph of a typical sample of a polycrystalline MCC deposited on a  $2.5 \times 2.5 \text{ cm}^2$  glass coverslip. Inset: A magnified portion of the sample that demonstrates how we performed image analysis to count domains and categorize sizes. Here, we have subtracted the background (tan regions in original image were replaced with black) and overlaid a gradient filter that outlines the borders of each region. B) Log-log plot of the distribution of areal density vs. domain size for the image shown in A. C) Histogram showing the percent of the sample area belonging to each of the clustered colors.

Figure S7B shows the collected statistics fitted to an inverse power law; we found that the areal density of domains  $n$  ( $\text{cm}^{-2}$ ) decayed with domain-area  $a$  ( $\text{mm}^2$ ) as  $n = 0.15a^{-1.70}$ . Figure S7C shows a histogram for the fractional area (%) covered by each type of domain (the fraction of pixels clustered into each of the 14 color bins relative the total number of pixels spanned by the sample). We do not count the “non-sample” regions that we masked. We found that nearly 80% of the sample was covered by single domains. The fractional areas of the 14 clustered domains were normally distributed around an average of  $6 \pm 2\%$  of the total area. This result suggests that different grain orientations are randomly distributed throughout the sample.

### **Design, Characterization, Modeling and Visualization of Structures**

We used SSL Artist to design all structures and simulated the transmission spectra of selected metasurfaces with the frequency domain package of CST Microwave Studio (CST). We used the optical constants in CST for the borosilicate substrate, and extrapolated the real and imaginary parts of the dielectric constants of Au and Ti from a the Brendel-Bormann analytic model.<sup>13</sup> We used an FESEM (Ultra Plus, Zeiss) to image all samples and an FT-IR spectrometer microscope (Lumos, Bruker) to characterize the infrared transmission spectra of selected metasurfaces fabricated on a borosilicate substrate. The unique shape of each domain enabled us to identify domains for characterization using the FESEM, and then to find them easily with the optical microscope attached to the FT-IR spectrometer. We used the edges of the samples to ensure identical alignment in both the FESEM and FT-IR measurements. We used an aperture-size  $100 \times 100 \mu\text{m}^2$  to characterize of the transmission spectra of chosen domains (each of which were 10–1000 times larger than the aperture). We generated the 3D renderings of spheres and shadows seen in Figures 1, 4, and S1 with MegaPOV (<http://megapov.inetart.net>), a version of the free ray-tracing software POV-ray.

## REFERENCES

- (1) Hulteen, J. C.; Van Duyne, R. P. Nanosphere Lithography: a Materials General Fabrication Process for Periodic Particle Array Surfaces. *J. Vac. Sci. Technol. A* **1995**, *13*, 1553–1558.
- (2) Haynes, C. L.; Van Duyne, R. P. Nanosphere Lithography: a Versatile Nanofabrication Tool for Studies of Size-Dependent Nanoparticle Optics. *J. Phys. Chem. B* **2001**, *105*, 5599–5611.
- (3) Zhao, J.; Frank, B.; Burger, S.; Giessen, H. Large-Area High-Quality Plasmonic Oligomers Fabricated by Angle-Controlled Colloidal Nanolithography. *ACS Nano* **2011**, *5*, 9009–9016.
- (4) Zhang, G.; Wang, D.; Möhwald, H. Fabrication of Multiplex Quasi-Three-Dimensional Grids of One-Dimensional Nanostructures via Stepwise Colloidal Lithography. *Nano Lett.* **2007**, *7*, 3410–3413.
- (5) Choi, Y.; Hong, S.; Lee, L. P. Shadow Overlap Ion-Beam Lithography for Nanoarchitectures. *Nano Lett.* **2009**, *9*, 3726–3731.
- (6) Vogel, N.; Fischer, J.; Mohammadi, R.; Retsch, M.; Butt, H.-J.; Landfester, K.; Weiss, C. K.; Kreiter, M. Plasmon Hybridization in Stacked Double Crescents Arrays Fabricated by Colloidal Lithography. *Nano Lett.* **2011**, *11*, 446–454.
- (7) Junesch, J.; Sannomiya, T.; Dahlin, A. B. Optical Properties of Nanohole Arrays in Metal–Dielectric Double Films Prepared by Mask-on-Metal Colloidal Lithography. *ACS Nano* **2012**, *6*, 10405–10415.
- (8) Cheung, C. L.; Nikolić, R. J.; Reinhardt, C. E.; Wang, T. F. Fabrication of Nanopillars by Nanosphere Lithography. *Nanotechnology* **2006**, *17*, 1339–1343.
- (9) Kostinski, S. V.; Chen, E. R.; Brenner, M. P. Characterization of Patterns Formed by Shadows of Spheres. *Phys. Rev. Lett.* **2014**, *112*, 235502–235502.
- (10) Vogel, N.; Goerres, S.; Landfester, K.; Weiss, C. K. A Convenient Method to Produce Close-and Non-Close-Packed Monolayers Using Direct Assembly at the Air–Water Interface and Subsequent Plasma-Induced Size Reduction. *Macromol. Chem. Phys.* **2011**, *212*, 1719–1734.
- (11) Sun, J.; Tang, C.-J.; Zhan, P.; Han, Z.-L.; Cao, Z.-S.; Wang, Z.-L. Fabrication of Centimeter-Sized Single-Domain Two-Dimensional Colloidal Crystals in a Wedge-Shaped Cell Under Capillary Forces. *Langmuir* **2010**, *26*, 7859–7864.
- (12) Sun, X.; Li, Y.; Zhang, T. H.; Ma, Y.-Q.; Zhang, Z. Fabrication of Large Two-Dimensional Colloidal Crystals via Self-Assembly in an Attractive Force Gradient. *Langmuir* **2013**, *29*, 7216–7220.
- (13) Rakic, A. D.; Djurišić, A. B.; Elazar, J. M.; Majewski, M. L. Optical Properties of Metallic Films for Vertical-Cavity Optoelectronic Devices. *Appl. Opt.* **1998**, *37*, 5271–5283.